Photoredox Nickel-Catalyzed C–S Cross-Coupling: Mechanism, Kinetics and Generalization

Yangzhong Qin,[‡] Rui Sun,[‡] Nikolas P. Gianoulis and Daniel G. Nocera*

Department of Chemistry and Chemical Biology, Harvard University, 12 Oxford Street, Cambridge, MA 02138

ABSTRACT: Photoredox mediated nickel-catalyzed cross-couplings have evolved as a new effective strategy to forge carbon-heteroatom bonds that are difficult to access with traditional methods. Experimental mechanistic studies are challenging because these reactions involve multiple highly reactive intermediates and perplexing reaction pathways, engendering competing, but unverified, proposals for substrate conversions. Here, we report a comprehensive mechanistic study of photoredox nickel-catalyzed C–S cross-coupling based on time-resolved transient absorption spectroscopy, Stern-Volmer quenching, and quantum yield measurements. We have (i) discovered a self-sustained productive Ni(I/III) cycle leading to a quantum yield $\Phi > 1$; (ii) found that pyridinium iodide, formed *in situ*, serves as the dominant quencher for the excited state photocatalyst and a critical redox mediator to facilitate the formation of the active Ni(I) catalyst; and (iii) and observed critical intermediates and determined the rate constants associated with their reactivity. The findings not only reveal a complete reaction cycle for C–S cross-coupling, but the mechanistic insights have allowed for the reaction efficiency to be optimized and the substrate scope to be expanded from aryl iodides to include aryl bromides, thus broadening the applicability of photoredox C–S cross-coupling chemistry.

Introduction

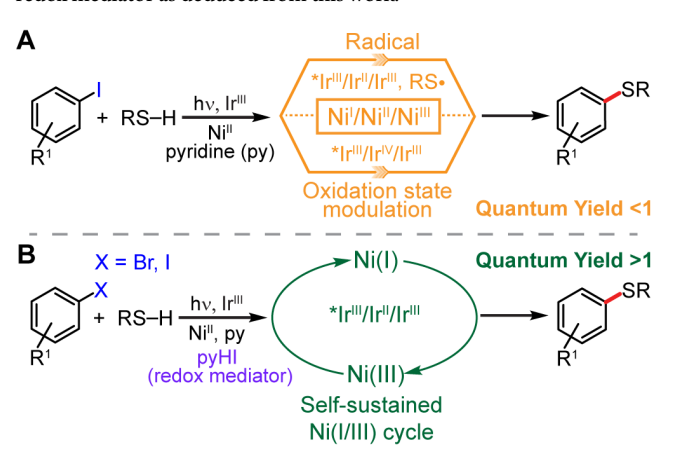
Photoredox generation of transition metal intermediates has emerged as a powerful strategy for promoting transformations that are otherwise difficult to access thermally. 1-8 A tandem approach of employing a photoredox catalyst to drive transition metal catalysis has been fruitful, 9-15 especially for effecting nickel-catalyzed carbonheteroatom bond formation under mild conditions using simple and inexpensive ligands at room temperature. 16-25 However, despite the prolific reports of new nickel photoredox methods, there have been relatively few experimental mechanistic studies due to reaction complexity.26-30 The variety of potential reaction pathways in photoredox cross-coupling systems together with the accessibility of multiple oxidation states obfuscate the precise redox chemistry between the photocatalyst and the cross-coupling catalyst, and consequently, the nickel redox levels responsible for supporting catalysis. Lacking such a mechanistic understanding can impede reaction development and optimization, which often rely on timeconsuming and labor-intensive trial-and-error reaction screening.

Thioethers are frequently encountered in natural bioproducts and pharmaceuticals. The potential bioactivity of thioethers in the treatment of diseases such as cancer and HIV³¹⁻³⁵ has motivated interest in developing effective methodologies for their synthesis.^{25,34-43} Recently, visible-light-driven photoredox nickel-catalysis has provided a new strategy to forge C–S bonds between (hetero)aryl iodides and thiols under mild conditions,²⁵ thus representing an important advance over traditional methods requiring high temperatures or strong bases.³⁴⁻³⁹ Unlike other photoredox nickel-catalyzed cross-couplings between aryl bromides and alcohols, amines, or carboxylic acids,²⁰⁻²² where the nucleophile engages the nickel catalyst through a redox-neutral metalation-deprotonation sequence, the coupling of aryl iodides to thiols has

been proposed to proceed through a 'radical' pathway via the photogeneration of thiyl radicals (Scheme 1A),25 thus circumventing the formation of free thiolate equivalents that are known to coordinatively inhibit catalysis. 16,35 Conversely, computational studies have suggested an alternative 'oxidation state modulation' mechanism (Scheme 1A) involving oxidative quenching of the excited iridium photocatalyst and the formation of a nickel thiolate from the deprotonation of coordinated thiol.⁴⁴ Both mechanisms invoke closed photocycles (quantum yield $\Phi < 1$) requiring the involvement of Ni(I), Ni(II), and Ni(III) intermediates for every turnover. 25,44 This is in contradistinction to recent investigations of photoredox-mediated nickel-catalyzed cross-coupling of aryl bromides with alcohols, 29,45,46 amines, 30,45,46 and carboxylic acids, 45 wherein $\Phi > 1$ owing to a self-sustained Ni(I/III) dark cycle have been discovered. Whether a self-sustained Ni(I/III) cycle is also responsible for aryl thiolation warrants investigation because a thermally-sustained cycle will involve unique reaction intermediates that engender optimization strategies distinct from both of the previously proposed mechanisms (Scheme 1A). 25,44

We now report a comprehensive mechanistic study on the photoredox mediated nickel-catalyzed C–S cross-coupling (Scheme 1B). Through a combination of time-resolved photophysical and photochemical techniques, we find that the photoredox mechanism is characterized by twelve rate constants associated with a thermally-sustained Ni(I/III) cycle with $\Phi > 1$. Nanosecond transient absorption spectroscopy permits the observation of the *in-situ* formation and subsequent reactivity of a Ni(I) intermediate, along with a side reaction leading to thiyl radical formation. Furthermore, we identify the hitherto underappreciated, but nonetheless critical, roles of pyridinium iodide (pyHI), which is produced as a byproduct of the cross-coupling. We show that pyridinium iodide is essential to facilitating the photoredox transformation by: (i) quenching the

Scheme 1. **(A)** Proposed mechanisms for photoredox mediated nickel-catalyzed aryl thiolation, and **(B)** self-sustained mechanism driven by a redox mediator as deduced from this work.



excited photocatalyst; (ii) preventing the formation of nickel thiolate complexes that competitively absorb light; and (iii) acting as a redox mediator to efficiently generate Ni(I) from off-cycle Ni(II) species, thereby sustaining a productive Ni(I/III) catalytic cycle. By leveraging these mechanistic insights, we present a strategy to expand the substrate scope of this methodology, which has been restricted to only aryl iodides, to include aryl bromides, allowing for access to a class of electrophiles with higher availability and lower cost.

Experimental

General Considerations. All samples were prepared in a nitrogen-filled glovebox with commercial reagents and anhydrous acetonitrile stored over activated 3 Å molecular sieves. Ir(III) (= [Ir(dF-CF₃-ppy)₂(dtbbpy)][PF₆] and dtbbpy= 4,4'-di-tert-butyl-2,2'-dipyridyl) was purchased from Strem Chemicals and used as received. Ni(II) (= (dtbbpy)NiCl2) was prepared in situ from (dme)NiCl₂ and dtbbpy, both of which were purchased from Sigma-Aldrich and used as received. Thiols were obtained from Oakwood Chemical. 1-Methylpyridinium iodide was prepared from a metathesis reaction between 1-methylpyridinium chloride and sodium iodide in acetonitrile. Typically, reaction solutions were stored in a 20-mL glass vial and sealed with electric tape. For convenience of presentation, Table 1 lists the compositions of key solutions used in this study. The photocatalytic reactions were carried out on solutions as reported previously25 except that, rather than purging the head space with nitrogen, all samples described herein were prepared in a glovebox. Additionally, in place of a 34W blue LED excitation source, solutions were illuminated with a Kessil A160WE Tuna Blue light source at a short distance (Figure S1A), and constantly agitated with a magnetic stirrer and cooled with a fan. For reactions at 55 °C, a hot plate equipped with a thermocouple was used. UV-vis spectra were measured with a Cary 5000 spectrometer (Agilent) and blank-corrected against the solvent. NMR spectra were recorded on an Agilent DD2 spectrometer (600 MHz) or a Varian/Inova spectrometer (500 MHz). The product yields were obtained based on the ¹H NMR spectra referenced to pre-quantified 1,3-benzodioxole as the internal standard.

Stern-Volmer Quenching Studies. Steady-state emission spectra were obtained using a fluorimeter (Photon Technology International, Model QM4). Steady-state Stern-Volmer quenching

Table 1. Composition of key solutions used in kinetics studies.

Solution	Composition
S1	Ni(II) (10 mM) + py (200 mM) + thiol 2 ^a (150 mM)
S2	$Ir(III)$ (150 μ M) + pyHI (25 mM)
S3	$S2 + py (200 \text{ mM}) + thiol 2^{a} (150 \text{ mM})$
S4	S3 + Ni(II) (10 mM)

a thiol **2** = 4-methoxybenzyl mercaptan

studies were carried out by measuring the steady-state emission intensity (I) at 500 nm and exciting the photocatalyst $\mathbf{Ir}(\mathbf{III})$ at 370 nm. The dynamic Stern-Volmer quenching studies were carried out by exciting solutions at 430 nm and measuring the lifetime (τ) of the photocatalyst excited state, * $\mathbf{Ir}(\mathbf{III})$, at 500 nm using the laser setup described below. The quenching ratio (I_0/I or τ_0/τ) and the Stern-Volmer constant (K_{sv}) were determined by the relation,

$$I_0/I \text{ or } \tau_0/\tau = 1 + K_{sv} [\text{quencher}]$$
 (1)

where I_0 and τ_0 are the emission intensity and lifetime in the absence of quencher, respectively. The quenching rate (k_q) is given by $k_q = K_{sv}/\tau_0$. Depending on the experimental conditions and the presence of adventitious oxygen in the sample, the measured τ_0 varies marginally (see Figure S4).

Reaction Progress and Quantum Yield Measurements.

Reaction solutions were prepared with acetonitrile-d₃ and stored in J. Young NMR tubes (1 mL each) in a N2-filled glovebox. For samples exposed to air, the screw cap of the NMR tube was opened for ~5 sec and then closed, and the solution was mixed by turning the NMR tube over repeatedly. This procedure was repeated two more times. All NMR tubes were placed in a 3-D printed NMR tube holder which was located at the center of the cylindrically-arranged 24 W blue LED strip lights (Figure S1B) to ensure that each sample receives the same amount of illumination. A fan was mounted at the top of the apparatus to cool the samples. The product yields were obtained at different times based on the ¹H NMR spectra. For quantum yield measurements, the output from a 150 W Xe arc lamp (Newport 67005 arc lamp housing and 69907 universal arc lamp power supply) was passed through a 435 nm band pass filter (FWHM = 10 nm) and a lens (f = 40 mm) was used to focus the light onto the reaction solution contained within a 1-cm cuvette. The power reaching the sample was attenuated by neutral density filters and measured with an Ophir ORION/PD power meter equipped with a PD-300-ROHS head sensor. The photon flux was calibrated against a potassium ferrioxalate standard based on a published procedure.47 Each quantum yield measurement was performed in triplicate.

Time-Resolved Emission and Transient Absorption Spectroscopy. A Quanta-Ray Nd:YAG laser (SpectraPhysics) produced laser pulses at 355 nm at a repetition rate of 10 Hz and a time width of 8 ns. The 355 nm laser pulses were either directly used or passed to a MOPO (SpectraPhysics) to produce laser pulses at 430 nm for sample excitation. A 75 W xenon-arc lamp (PTI, Model A1010) was used to generate white probe light for transient absorption (TA) measurements. Both excitation and probe beams were focused and overlapped onto the sample, which was typically contained in a 1-cm cuvette. The emission of the photocatalyst and the transmitted probe light were directed to a Triax 320 spectrometer and the signal was detected with a photomultiplier

Table 2. Photoredox mediated nickel-catalyzed aryl thiolation and Stern-Volmer quenching studies. ^a

Reagent	K _{SV} / M ⁻¹ (steady-state)	K _{SV} / M ⁻¹ (dynamic)	k _q / M ⁻¹ s ⁻¹ (dynamic)
pyridine (py) b	-	-	-
Ni(II)	N.A. ^c	200(8)	$7.8(3) \times 10^7$
1a	1.5(1)	1.3(1)	5.1(4) x 10 ⁵
2	1.9(1)	2.4(2)	1.1(1) x 10 ⁶
2 with py	7.1(4)	7.6(5)	3.4(2) x 10 ⁶
руНІ	53383(3370)	54480(2243)	2.1(1) x 10 ^{10 d}

 $[^]a$ All reagent concentrations are referenced to a 0.1 M concentration of **1a**. b No quenching observed. c Not measured. d kq,ET in kinetic modelling.

tube (PMT) (Hamamatsu) coupled to a 1 GHz oscilloscope (LeCroy, Model 9384CM) or a CCD camera (Andor Technology). Further details of the laser spectroscopic setup can be found elsewhere.⁴⁸ The fitting models for the TA kinetic traces are provided in the Supporting Information.

UV-vis Study with (dtbbpy)NiCl₂ in the Presence of Thiolate. A 50-mL glass bottle was charged with (dme)NiCl₂ (43.9 mg, 0.200 mmol) and dtbbpy (80.5 mg, 0.300 mmol). MeCN (20 mL) was then added and the reaction mixture was stirred for 30 min at room temperature to form Ni(II). A 5 mL aliquot was drawn and added to a 20-mL scintillation vial charged with potassium (4-methoxyphenyl)methanethiolate (4.8 mg, 0.025 mmol), which was prepared from the corresponding thiol and potassium *tert*-butoxide, and the reaction mixture was stirred at room temperature for 2 h. The mixture was then filtered using a 0.2-μm PTFE syringe filter and diluted 10 times with MeCN. A UV-vis spectrum was recorded on the resulting solution.

Results

Quenching Studies. We undertook mechanistic investigation of the C-S cross-coupling by examining which reagents listed in Table 2 react with *Ir(III) per steady-state and dynamic Stern-Volmer quenching. Pyridine does not quench ***Ir**(**III**) (Figure S2). In the case of Ni(II), the steady-state K_{sv} cannot be accurately measured due to its strong and broad absorption, which overlaps with that of Ir(III) and thus requires inner-filter corrections (Figure S3 and Section B.1 in the SI). Steady-state Stern-Volmer quenching plots for reagents in Table 2 are shown in Figure S4. Ni(II) shows dynamic quenching with a rate constant of $k_q = 7.8(3) \times 10^7 \text{ M}^{-1} \text{ s}^{-1}$, which is ~2 orders of magnitude greater than that of any other individual component in the original reaction solution, including 4iodotoluene (1a) and 4-methoxybenzyl mercaptan (2) (Table 2). Thiol compound 2 in the presence of 200 mM pyridine exhibits a quenching rate ~3 times higher than that of 2 alone. However, when concentrations of the reactants are considered, the overall contributions to the quenching of *Ir(III) by the reactants (Ni(II), 1a and 2) in the starting solution are comparable. The lifetime of *Ir(III) in the reaction solution can be explicitly determined by monitoring the compound's emission decay at 500 nm ($\lambda_{exc} = 430$

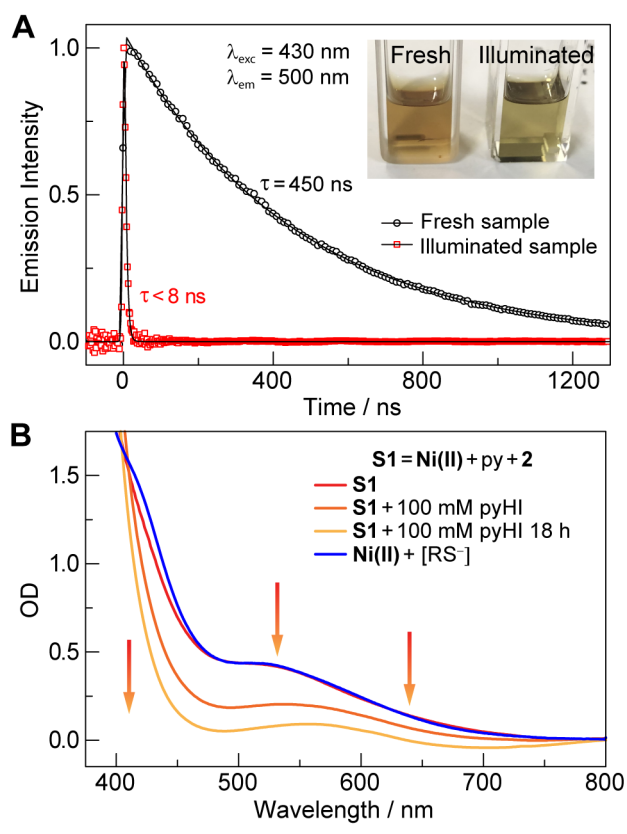


Figure 1. (**A**) Time-resolved emission decay of the excited photocatalyst ***Ir**(**III**) in a fresh and illuminated sample, the latter of which was subjected to 20 min blue light irradiation under standard reaction conditions (Table 2, top panel). The scatter plots and solid lines show the raw data and single-exponential fittings, respectively. The fitted lifetime τ is significantly lower for an illuminated sample when compared to a fresh one. This change in ***Ir**(**III**) lifetime is accompanied by a change in the color of the reaction solution, as shown in the inset. (**B**) UV-vis absorption spectra of solution **S1** (Table 1), and with 100 mM pyHI at 0 h and 18 h in the dark, and a solution containing **Ni**(**II**) with RS $^-$ (potassium (4-methoxyphenyl)methanethiolate), the spectrum for which is normalized with that of **S1** at 500 nm.

nm). For a fresh reaction solution, the measured lifetime was $\tau = 450$ ns (Figure 1A). However, for a solution that was illuminated for 20 min under blue light, the lifetime fell below our instrumental time resolution (8 ns), indicating the in-situ generation and accumulation of a byproduct that was an efficient quencher. Control experiments based on the ¹⁹F spectra (Figure S13) for solutions before and after illumination showed no appreciable change, suggesting that Ir(III) is stable during the reaction and the lifetime change is not due to nonradiative pathways associated with photocatalyst degradation. In particular, the presence of an iodide substrate, thiol as a proton source (from its acid-base chemistry and PCET involvement in photoredox reactions⁴⁹⁻⁵¹) and pyridine suggests the possibility of generating pyridinium iodide (pyHI). As shown in Table 2, pyHI is an exceptional quencher of *Ir(III); the quenching rate constant of $k_{\rm q,ET} = 2.1(1) \times 10^{10} \,\mathrm{M}^{-1}\,\mathrm{s}^{-1}$ is over 2 orders of magnitude higher than that of Ni(II). A similar quenching rate was obtained for tetrabutylammonium iodide (TBAI) (Figure S4D), suggesting that this unusually high quenching rate constant is due to the photooxidation of iodide (I⁻) by *Ir(III).

Effect of Thiolate and pyHI on (dtbbpy)NiCl₂. The initial reaction solution was orange (Figure 1A, inset), which we later discovered was similar to the color of solution S1 (S1 = 10 mM Ni(II), 200 mM pyridine and 150 mM thiol 2 in MeCN). To identify the compound responsible for the orange color, we prepared a solution of Ni(II) in the presence of potassium (4-methoxyphenyl)methanethiolate. The UV-vis absorption spectrum of this solution (Figure 1B, blue trace) is nearly identical to that of solution S1 (Figure 1B, red trace), suggesting that the orange color is due to a nickel thiolate compound. When the complete reaction solution (Table 2, top) was photolyzed, the initial orange color gradually disappeared and the solution turned yellow (Figure 1A, inset), diagnostic of Ir(III) solutions. This result suggested protonolysis of the nickel-thiolate complex present in the initial solution. We hypothesized that the Brønsted acid pyHI is responsible for this protonolysis reaction and that this acid accumulated as the reaction progressed. Indeed, addition of 100 mM pyHI to solution S1 prompted a color change (Figure 1B, red to red-orange trace) that continued to lighten in color over 18 h of storage in the dark (Figure 1B, orange trace). Additionally, if pyHI was added to the initial reactant solution before thiol, the orange color, indicative of the nickel-thiolate, was not observed. These results suggest that pyH^+ ($pK_a = 3.4$ in DMSO)⁵² can protonate any thiolate equivalents formed in situ, thereby avoiding the formation of the nickel thiolate complex, which can cause a strong inner filter effect.

Reaction Progress and Quantum Yield Measurements.

The effect of pyHI on the C–S cross-coupling between 1a and 2 was examined under different conditions by monitoring the product yield with time (Figure 2A, details provided in Experimental Section). Under reaction conditions similar to those of the published method, ²⁵ where O_2 was present, the reaction showed an induction period in the first 20 min (Figure 2A, black trace) that was more prominent for an identical sample when exposed to air (Figure 2A, red trace). However, the induction period diminished after adding 50 mM pyHI (Figure 2A, blue and teal traces). The sample without air exposure exhibited the highest initial photoreaction rates (Figure 2A, blue trace). Although the product yield (Figure 2A) is within error and not distinguished at the early stages of reaction (≤ 6 min), a clear overall trend is established at later times of reaction (at times > 6 min) that lies well outside the standard deviation of 5-15 % as reflected in the quantum yield measurements (Figure 2B).

To further quantify the reaction efficiency and gain mechanistic insight, we measured the quantum yield for the C-S cross-coupling with and without pyHI (Figure 2B, black and grey traces). The addition of pyHI (50 mM) results in an increase in the quantum yield by 50% (from 0.12(2) to 0.18(1)) with an incident power of 7.4 mW. The quantum yield also increases with decreasing incident power of the irradiation source; changing the incident power from 7.4 mW to 90 µW results in a 375% increase in quantum yield (from 0.12(2) to 0.45(3) in the absence of pyHI), which is accentuated in the presence of pyHI (increase of 594%, from 0.18(1) to 1.07(11)). A quantum yield in excess of 1 ($\Phi > 1$) was further corroborated by using 4'-iodoactophenone as a substrate (Figure 2B, red trace). With this more electron-deficient aryl halide, the quantum yield increases from 0.28(2) at 7.4 mW to 2.04(6) at 90 µW. Significantly, these values of $\Phi > 1$ establish the existence of a thermally selfsustained catalytic cycle^{29,45,46} for product formation (vide infra).

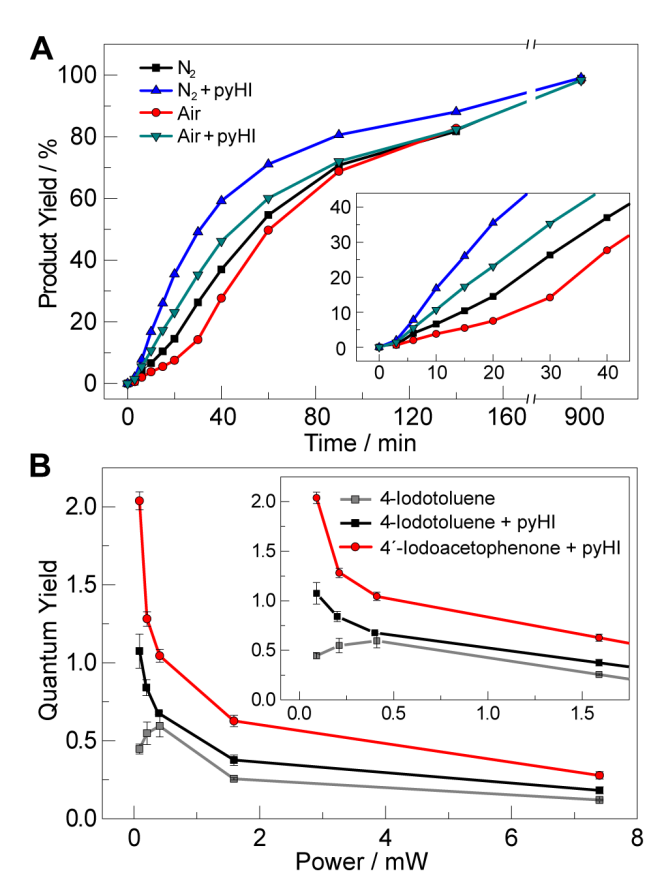


Figure 2. (**A**) Aryl thiolation progress for a standard reaction solution with the addition of 50 mM pyHI, exposure to air, or both. (**B**) Power dependence of the quantum yield for aryl thiolation between 4-methoxybenzyl mercaptan and 4-iodotoluene (**1a**) or 4'-iodoacetophenone with and without additional 50 mM pyHI (λ_{exc} = 435 nm). Lines are included to highlight the trend.

Transient Intermediates and Reaction Kinetics.

Nanosecond TA spectroscopy was employed to interrogate the photoredox process as well as identify reaction intermediates and define the kinetics of a complete photoredox cycle. Upon addition of 25 mM pyHI or TBAI to a solution of 150 μM Ir(III), TA features at ~400, 525 and 720 nm were observed 30 ns after photoexcitation (Figure 3A). The TA spectrum consist of two components (Figure 3A, inset): the reduced photocatalyst, Ir(II), and $I_2 \bullet^-$. The spectrum of Ir(II) (maxima at 400 and 525 nm) has been previously determined by spectroelectrochemistry.²⁹ Subtraction of the Ir(II) spectrum from the TA spectrum recorded at 30 ns yields the blue trace (Section B.2 in SI), which matches that of $I_2 \bullet^-$ (maxima at 395 and 720 nm). 53 These results confirm that I quenches *Ir(III) by electron transfer to form Ir(II) and I., the latter of which reacts facilely with I^{-.53} Based on the Stern-Volmer quenching study (Table 2), the electron transfer rate between *Ir(III) and I^- is $k_{q,ET}$ = $2.1(1) \times 10^{10} \text{ M}^{-1} \text{ s}^{-1}$.

In addition to the role of iodide, we also investigated the role of pyH $^+$. The TA spectrum for solution S2 (S2 = 150 μ M Ir(III) + 25 mM pyHI) shows clear distinctions in time evolution for Ir(II) as compared to when pyHI was replaced with TBAI (Figure 3A). For the solution with TBAI, the TA features at 525 nm (predominantly Ir(II)) and 720 nm (predominantly I $_2 \bullet^-$) both decay at a similar rate, suggesting a clean back electron transfer reaction between I $_2 \bullet^-$ and Ir(II) to form 2I $^-$ and Ir(III). However, with pyHI, the TA

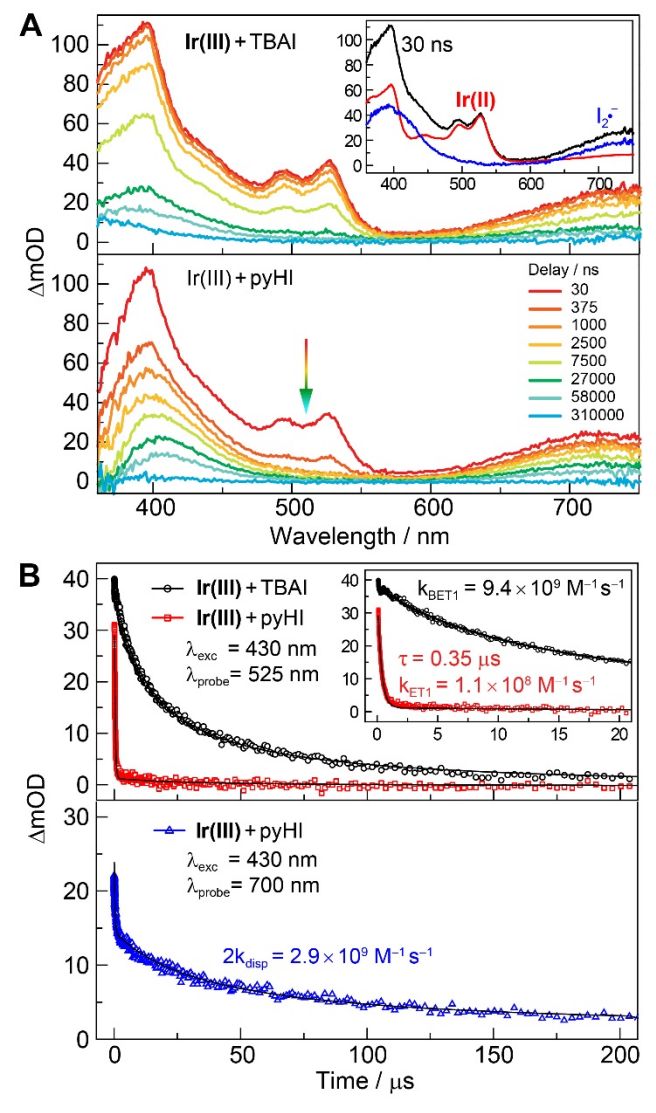


Figure 3. (**A**) TA spectra of a solution containing 150 μM **Ir(III)** and 25 mM TBAI or pyHI ($\lambda_{\rm exc}$ = 430 nm). The inset shows that the corresponding TA spectrum at 30 ns can be deconvolved into contributions from **Ir(II)** (red) and I₂•⁻ (blue). The delay times listed in the bottom panel also apply to the top panel. (**B**) The TA kinetic traces probed at 525 nm and 700 nm predominantly show the decay of **Ir(II)** and I₂•⁻, respectively. The scatter plots and the solid lines show the raw data and model fittings, respectively (see SI for details).

feature at 525 nm (Ir(II)) decays much faster than that at 720 nm ($I_2 \bullet ^-$), suggesting that the disappearance of Ir(II) is predominantly due to the reaction between Ir(II) and pyH $^+$ to form Ir(III) and pyH $^+$. Similarly, in the presence of 1-methylpyridinium iodide, a faster decay of Ir(II) was also observed (Figure S5), ruling out the possibility that the reaction between Ir(II) and pyH $^+$ required a proton. By monitoring the decay of Ir(II) at 525 nm with TBAI as the quencher, we extracted a rate constant for the back electron transfer reaction between $I_2 \bullet ^-$ and Ir(II) (Figure 3B, black curve and Section B.3.1 in the SI) of $I_{BETI} = 9.4(2) \times 10^9 \, M^{-1} \, s^{-1}$, consistent with an appreciable driving force ($I_{1/2}(Ir(II/III)) = -1.74 \, V^{29}$ and $I_{1/2}(I_2 \bullet ^-/I^-) < 0.30 \, V^{54} \, vs \, Fc^+/Fc$). For the case of pyHI (Figure 3B, red curve), and accounting for $I_{BETI} = 1.14(3) \times 10^8 \, M^{-1} \, s^{-1}$ is extracted for the reaction between pyH $^+$ and Ir(II), which is also

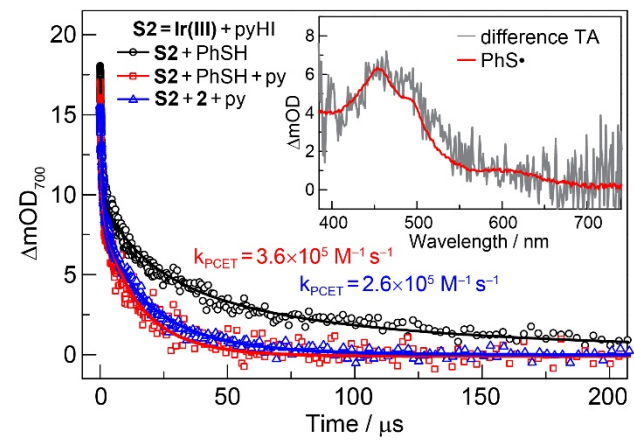


Figure 4. TA kinetic trace probed at 700 nm for solution **S2** (150 μM **Ir(III)** and 25 mM pyHI) with 150 mM thiophenol, 150 mM thiophenol in the presence of 200 mM pyridine, and 150 mM 4-methoxybenzyl mercaptan in the presence of 200 mM pyridine (λ_{exc} = 430 nm). The faster decay for solutions containing pyridine is due to PCET between I₂• and thiol with pyridine as a base. The scatter plots and solid lines show the raw data and model fittings, respectively (see SI for details). The inset shows the difference TA spectrum at 6.3 μs (grey) for solutions of **S2** with 150 mM thiophenol in the absence and presence of 200 mM pyridine; this difference spectrum matches the TA spectrum of thiophenoxyl radical (red) obtained independently from directly exciting diphenyl disulfide at λ_{exc} = 355 nm.

thermodynamically favored ($E^{\circ} = -1.7 \text{ V}$ vs Fc^{+}/Fc for the pyH⁺/pyH• couple, ^{55,56} where 0.4 V was used to convert reference potential from SCE to Fc^{+}/Fc). Note, despite k_{BET1} being nearly two orders of magnitude larger than k_{ET1} , we observed faster reaction of Ir(II) with pyH⁺ than with $I_{2}\bullet^{-}$ due to the higher concentration of pyH⁺ (25 mM pyH⁺ versus less than 10 μ M $I_{2}\bullet^{-}$). Additionally, $I_{2}\bullet^{-}$, monitored at 700 nm (Figure 3B, blue curve), decays more slowly for the solution containing pyHI versus one containing TBAI due to the fast disappearance of Ir(II) in the former, which attenuates the back reaction between $I_{2}\bullet^{-}$ and Ir(II). Since $I_{2}\bullet^{-}$ is known to disproportionate, we attribute the slower decay at 700 nm to the disproportionation of $I_{2}\bullet^{-}$ to form I_{3}^{-} and I^{-} , for which we extracted a rate constant of $2k_{disp} = 2.9(1) \times 10^{9} \text{ M}^{-1} \text{ s}^{-1}$ (Section B.3.2 in the SI), consistent with reported rate constants. ^{53,57}

With the reaction and kinetics for solution S2 as a reference, the kinetics of S2 solutions containing more components of the C-S cross-coupling reaction were examined. The addition of 150 mM thiol 2 to solution S2 resulted in little change to the TA spectra and kinetics (Figures S6 and S7). However, the addition of both 200 mM pyridine and 150 mM 2 to solution S2, resulting in solution S3 (= S2 + 150 mM 2 + 200 mM py), accelerates the decay of $I_2 \bullet^-$ (Figure 4). We posit that the faster decay may result from proton-coupled electron transfer (PCET) between compound 2 and I2. in the presence of pyridine as a base to form thiyl radical 2., 2I and pyH+, which may occur in either a concerted or a stepwise fashion.^{58,59} To assess this contention, we chose to replace 2 in \$3 with thiophenol (PhSH) because the PhS• radical exhibits absorption in the visible region, allowing us to observe the radical product if PCET does indeed occur. The inset of Figure 4 shows the difference of TA spectra measured at 6.3 µs between solutions of S2 + 150 mM PhSH in the absence and presence of 200 mM pyridine (Figures S7A and

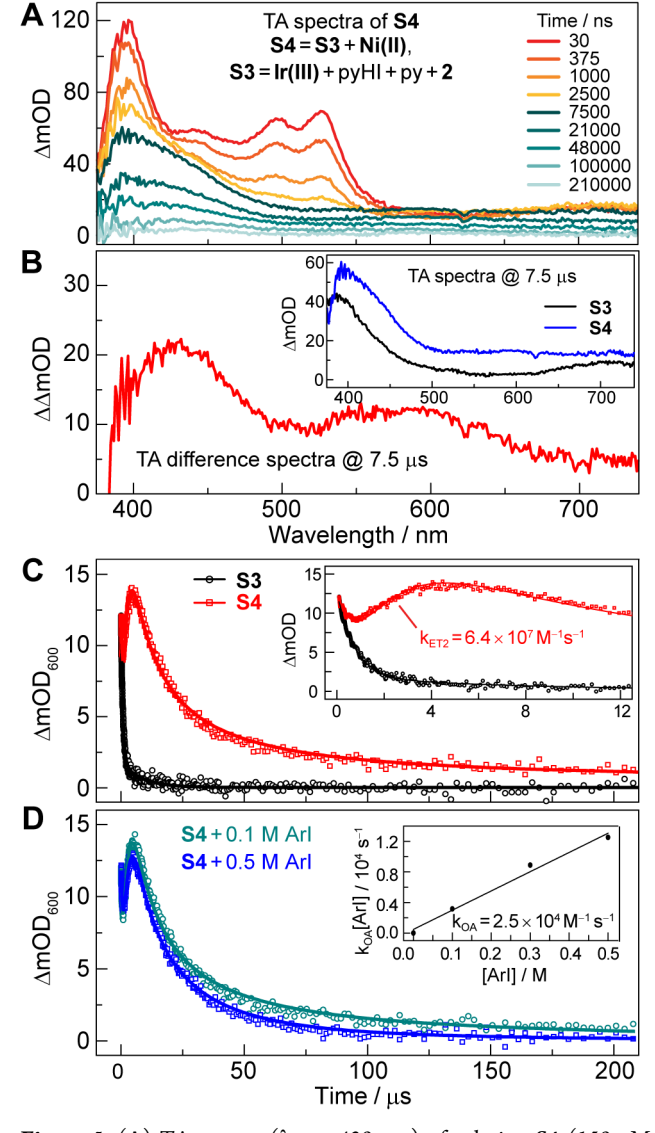


Figure 5. (**A**) TA spectra ($\lambda_{\rm exc}$ = 430 nm) of solution **S4** (150 μM **Ir(III)**, 25 mM pyHI, 200 mM pyridine, 150 mM 4-methoxybenzyl mercaptan, and 10 mM **Ni(II)**). (**B**) The difference TA spectrum at 7.5 μs for solution **S3** and **S4** (parent spectra shown in the inset), revealing the presence of a putative **Ni(I)** intermediate. (**C**) TA kinetic trace measured at 600 nm for solution **S3** (black) and **S4** (red). The additional rising feature on the red curve suggests the formation of **Ni(I)** with a time constant of 1.56 μs. (**D**) TA kinetic trace measured at 600 nm for solution **S4** with 0.1 and 0.5 M 4-iodotoluene, **1a**. The faster decay for solutions with higher concentrations of aryl iodide implies the oxidative addition of aryl iodide to the **Ni(I)**. The scatter plots and solid lines show the raw data and model fittings, respectively (see SI for details). The inset shows the linear fit to extract the oxidative addition rate constant k_{OA} of 4-iodotoluene, **1a**.

S7B, respectively); subtracting the spectrum without pyridine from that with pyridine furnishes a spectral profile (Figure 4 inset, grey trace and Figure S7C) with a band maximum at 450 nm, which is similar to the absorption profile of the PhS• radical (Figure 4 inset, red trace) as obtained independently by photolyzing a solution of 6 mM diphenyl disulfide (PhSSPh) with laser pulses at 355 nm. The PCET rate constants for thiol oxidation were derived to be $k_{\rm PCET}$ = $2.6\,(1)\times10^5\,{\rm M}^{-1}\,{\rm s}^{-1}$ for thiol 2 and $k_{\rm PCET}$ = $3.6(1)\times10^5\,{\rm M}^{-1}\,{\rm s}^{-1}$ for PhSH (Section B.3.3 in the SI). The observation of the thiyl radicals

by TA is consistent with their presence in C–S cross-coupling, as ascertained from radical trapping studies.²⁵

We next interrogated the role of Ni in the photoredox cycle by adding 10 mM Ni(II) to S3 (S4 = S3 + 10 mM Ni(II)). The measured TA spectra for solution S4 is shown in Figure 5A. Subtracting the TA spectrum of solution \$3 at 7.5 µs from that of \$4 yielded the difference TA spectrum (Figure 5B), which clearly shows two absorption features with maxima at 425 and 600 nm. These spectral features have been observed previously in photoredox aryl etherification 29 and arise from a Ni(I) intermediate. To further assess our assignment of the absorption bands in Figure 5B to a Ni(I) intermediate, we monitored the comproportionation between Ni(0) [Ni(0) = (dtbbpy)Ni(cod)] and Ni(II) (Section A.2 in the SI). Electron paramagnetic resonance (EPR) measurement of the comproportionation product supported the presence of a new Ni(I) species (Figure S8A). Furthermore, the comproportionation solution showed an absorption spectrum (Figure 8B) distinct from that of Ni(0) or Ni(II) (Figure S8C), with an absorption band in the 600 nm region. Exposure of the same solution to air led to the disappearance of the 600 nm band to give the Ni(II) absorption spectrum. To assess whether the Ni(I) species formed by the comproportionation reaction accounts for the TA difference spectrum shown in Figure 5B, the difference absorption spectrum for comproportionated solutions before and after air exposure (i.e., Ni(I) spectrum - Ni(II) spectrum) was computed (Figure S8D) and found to be similar to the difference TA spectrum shown in Figure 5B (red curve), thus supporting the formation of Ni(I) under photoredox conditions.

Accordingly, the kinetics of the Ni(I) intermediate, for which the 600 nm band offered a direct signature, were defined. Figure 5C shows the decay kinetics for the 600-nm signal of solution S4. A slight decay in signal over 0.5 µs is followed by a rise over 5 µs and then a subsequent slow decay lasting several hundreds of microseconds (Figure 5C, red trace). This evolution of the signal contrasts the immediate drop in signal at 600 nm observed for solution S3 (Figure 5C, black trace) where no nickel complex was present. An additional control experiment on a similar solution without thiol 2 but with the Ni(II) complex (S4 – 150 mM 2) also showed a decay-rise-decay feature, suggesting that the formation of Ni(I) species is not due to thiol 2 (Figure S9D, black trace). Significantly, the initial fast decay and slow rise indicate that the formation of Ni(I) occurs through the action of an intermediate that is not Ir(II), as its formation is slower than the disappearance of Ir(II). This result establishes that Ni(I) is not generated from the direct reduction of Ni(II) by Ir(II). As noted in Figure 3A, pyH• is present during the photoredox transformation and thus may act as a reductant for Ni(II). Consistent with this contention, the rate constant for the reaction between pyH• and Ni(II) was determined to be $k_{ET2} = 6.4(5) \times 10^7 \,\text{M}^{-1} \,\text{s}^{-1}$ whether in the presence or absence of thiol (Section B.3.4 in the SI). From modelling (Section B.3.5 in the SI) the slow decay over 5 to 200 μ s, $k_{BET2} = 8.5(4) \times 10^9 \,\text{M}^{-1} \,\text{s}^{-1}$, is ascribed to the back reaction between Ni(I) and I2. to form Ni(II) and $2I^-$.

Given the reported reduction potential for $\mathbf{Ir}(\mathbf{II})$ ($E_{1/2} = -1.74 \,\mathrm{V}$ vs Fc^+/Fc), 29 it should be able to directly reduce $\mathbf{Ni}(\mathbf{II})$ in the absence of pyH $^+$. To test this hypothesis, we obtained the TA spectrum of a solution containing 150 μ M $\mathbf{Ir}(\mathbf{III})$, 25 mM TBAI, 200 mM py, and 10 mM $\mathbf{Ni}(\mathbf{II})$. We monitored the absorption maximum of $\mathbf{Ir}(\mathbf{II})$ at 525 nm, which was generated immediately

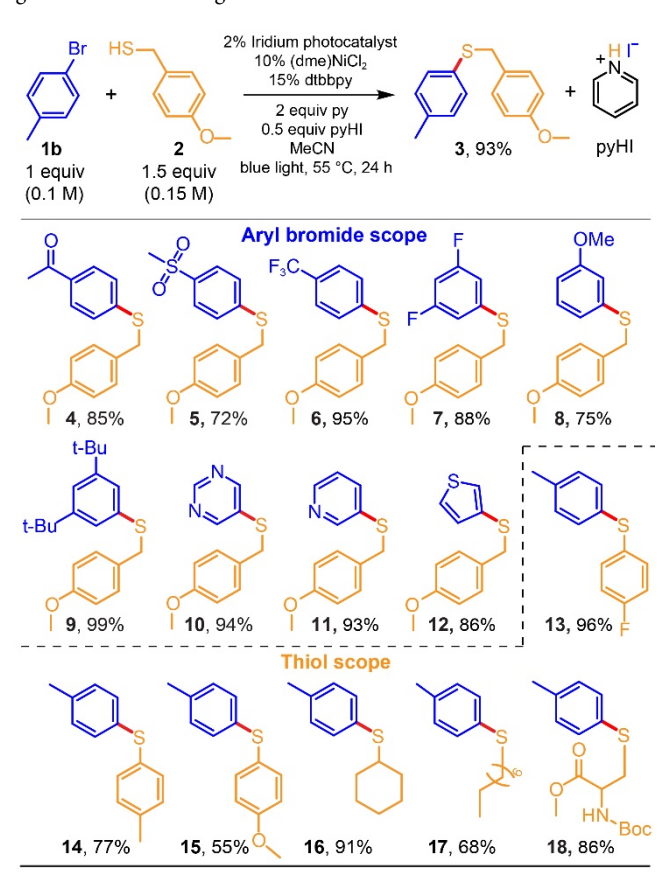
following the initial quenching and then decayed slowly due to the back reaction (Figures S9A and A9B, red curves). Monitoring Ni(I) at 600 nm, a decay-and-rise feature was not observed on a short time scale (< 5 μ s) (Figure S9D, red trace). However, an additional TA feature appeared on a longer time scale (>50 μ s) after Ir(II) and $I_2 \bullet^-$ had decayed significantly (shown by the comparison of the red curves in Figures S9C and S9D). This additional TA feature is likely due to the reaction between Ir(II) and Ni(II) in the presence of pyridine to form Ir(III) and Ni(I), the rate constant of which was extracted to be $k_{ET3} = 2.5(5) \times 10^6 \, M^{-1} \, s^{-1}$ (Figure S10 and Section B.3.5 in the SI).

The rate constant for the direct reduction of Ni(II) by Ir(II) in the presence of pyridine is much smaller than that of the pyH• mediated process. However, in the absence of pyridine, Ir(II) can effectively reduce Ni(II) directly to form Ni(I) with a rate constant of $k_{ET4} = 3.0(4) \times 10^7 \, \text{M}^{-1} \, \text{s}^{-1}$ (Figure S11 and Section B.3.5 in the SI). These results suggest that pyridine makes Ni(II) less amenable towards reduction. Indeed, the absorption spectrum of Ni(II) showed clear differences with and without 200 mM pyridine (Figure S12A). We further carried out cyclic voltammetry (CV) measurements on Ni(II) in the absence and presence of 200 mM pyridine. Despite the irreversibility of the reduction wave, its onset shifted cathodically by ~200 mV when pyridine was present (Figure S12B), consistent with the smaller reduction rate (k_{ET3}) observed for Ni(II) in the presence of pyridine.

With the formation pathways of Ni(I) determined, we further probed its oxidative addition (OA) reactivity⁶⁰ with 4-iodotoluene (1a) by monitoring the TA kinetics of Ni(I) at 600 nm. The Ni(I) decay became faster when the concentration of 1a was increased from 0 M to 0.5 M (Figures 5C and 5D). Specifically, with 0.5 M 1a, the signal drops to nearly zero after 100 µs. With fitting (Section B.3.4 in the SI), we extract the apparent OA rate constant, $k_{OA}[ArI]$, as a function of the aryl iodide concentration (Figure 5D, inset), where the slope of the linear fit furnishes a bimolecular OA rate constant of $k_{OA} = 2.5(2) \times 10^4 \text{ M}^{-1} \text{ s}^{-1}$. We emphasize that the obtained rate (k_{OA}) may offer an upper limit for the OA if other unknown reactions exist between Ni(I) and ArI. Given the quantitative product yield and high observed quantum yields (Figure 2), OA is likely the major reaction here. The observed k_{OA} is also consistent with previously reported values, 61 despite the differences of the specific ligand environment. Due to the absence of any salient signals in the TA spectrum, we were unable to measure the rates of ligand exchange or reductive elimination at Ni(III) following OA.

Reaction Optimization and Generalization. In line with previous observations, ²⁵ we found that the substrate scope for the C-S cross-coupling reaction was limited to aryl iodides (Table S1) under the conditions shown in Table 2. Guided by our mechanistic insights, which show the important, but previously unidentified, roles of pyridinium and iodide in the photoredox cycle, we found that the addition of pyHI and a slightly elevated temperature of 55 °C enables the C-S cross-coupling between 4-bromotoluene (1b) and thiol 2 (Table 3, top). Similarly, high yields were also obtained when TBAI was added since pyH⁺ is able to be generated *in situ* (Table S1). Finally, after testing multiple aryl bromides and thiols (Table 3, bottom). The optimized strategy applied well to aryl bromides with electron withdrawing groups (4-8), electron donating groups (1b, 9), and aryl heterocycles (10-12). Aryl thiols (13-15) and alkyl thiols (2, 16-18) were also well accommodated by

Table 3. Photoredox mediated nickel-catalyzed aryl thiolation using aryl bromide. Top panel shows the reaction used in photochemical kinetics studies with the bromo analogue of **1a**; bottom panel shows generalization to a range of substrates.



the strategy. Moreover, the amino acid cysteine (18) shows a high yield, indicating potential applicability for biomolecule preparation. Therefore, the generality of our optimization strategy was confirmed.

Discussion

Figure 6 summarizes the elementary reactions, reaction intermediates, and critical rate constants for a comprehensive description of the photoredox nickel-catalyzed cross-coupling between aryl halides and thiols. The productive reaction pathway consists of the following steps: (i) photoexcitation of Ir(III) to generate *Ir(III); (ii) reductive quenching of *Ir(III) by I to generate Ir(II) and I. (Figure 6, red cycle); (iii) reduction of pyH⁺ by Ir(II) to generate a pyridyl radical pyH• and Ir(III); (iv) reduction of the Ni(II) precatalyst by pyH• to form a Ni(I) species (Figure 6, blue cycle); (v) oxidative addition of anyl halide to Ni(I)to form a putative Ni(III) aryl halide complex and (vi) ligand exchange on Ni(III) and subsequent reductive elimination to release product and reform Ni(I) (Figure 6, green cycle). In addition to the major pathway of generating Ni(I) from step (iii), a minor pathway was also identified that (vii) generates Ni(I) from the direct reaction between Ir(II) and Ni(II).

The important role of the reactivity of downstream products originating from photogenerated I• is shown in the orange cycle of Figure 6. Following the initial quenching, I• complexes with I⁻ to form I₂• $^{-,53}$ which reacts with **Ir(II)** or **Ni(I)** via back electron

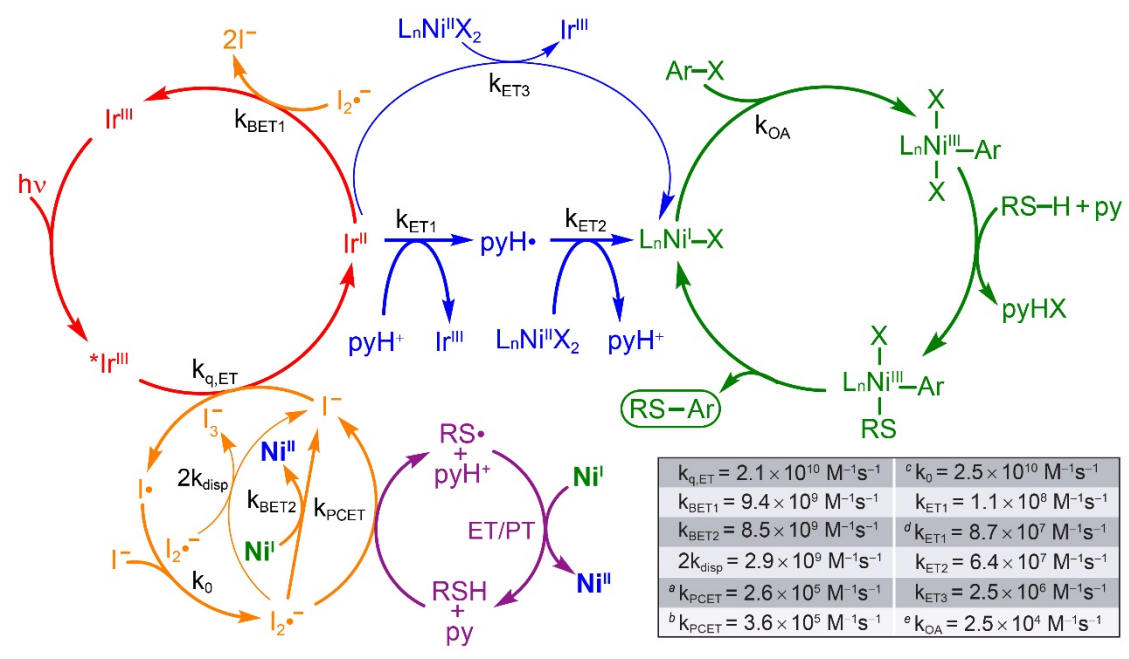


Figure 6. Complete reaction mechanism and key rate constants for photoredox mediated nickel-catalyzed aryl thiolation. ^a PCET reaction between $I_2 \bullet^-$ and compound **2.** ^b PCET reaction between $I_2 \bullet^-$ and thiolphenol. ^c Rate was reported by ref 53. ^d For the reaction with 200 mM pyridine. ^c Oxidative addition of 4-iodotoluene. **Ni**^{II} = I_n Ni^{II}X2; **Ni**^{II} = I_n Ni^{IX}X. ET = electron transfer; PT = proton transfer.

transfer, leading to the deactivation of these two key intermediates. Alternatively, $I_{2\bullet}^-$ may oxidize thiol in the presence of pyridine via PCET to generate a thiyl radical and pyH⁺, both of which eventually undergoes back reaction with Ni(I) in what is likely a multi-step process involving electron and proton transfer (Figure 6, purple cycle). Additionally, $I_{2\bullet}^-$ can also disproportionate to I^- and I_3^- (Figure 3B), the latter of which can also oxidize Ni(I). However, under actual reaction conditions, this disproportionation becomes negligible given the fast back electron transfer and PCET reactions.

The mechanism we have elucidated herein highlights the importance of accessing and perpetuating a thermally-sustained and productive Ni(I/III) cycle, which is evidenced by the larger-thanone quantum yields observed at low powers (Figure 2B). Due to the bimolecular nature of all the back-electron transfer reactions, the overall energy efficiency will decrease due to higher concentrations of the intermediates being generated at higher excitation powers. This was indeed observed, as the quantum yield increased significantly as the power of the excitation source was diminished (Figure 2B). Such an observation is in line with our previous results for photoredox aryl etherification, where the Ni(I/III) cycle is enhanced as the deactivation of the on-cycle nickel intermediates is attenuated at lower powers.²⁹ However, the photoredox aryl etherification and the C-S cross-coupling reaction reported here access the on-cycle Ni(I) catalyst in distinct ways. The direct reduction pathway, which is predominant in aryl etherification, becomes inefficient for generating Ni(I) in C-S cross-coupling due to the retarded reaction (ket3) between Ir(II) and Ni(II) as compared to the competing back reaction (kBET1) between Ir(II) and I2. (Figures 3 and S10). The pyH+ that is formed in situ provides an efficient pathway to transport electrons from Ir(II) to Ni(II) through pyH⁺/pyH• mediators to form Ni(I), and hence sustain the productive Ni(I/III) cycle (Figure 6). Although pyH⁺ has often been used as a redox mediator in CO₂ reduction^{55,56,62,63} and, recently, in nickel-catalyzed aryl amination with catalytic amounts of Zn metal as a reductant, 64 our discovery reveals an underappreciated role of pyH $^+$ as a viable mediator in photoredox chemistry.

The mechanism in Figure 6 differs from the previously reported 'radical' and 'oxidation state modulation' mechanisms^{25,44} (Scheme 1A) in critical ways. These mechanisms propose the production of Ni(I) by reduction of Ni(II) for each turnover in the cycle. This restricts the quantum yield to be $\Phi \leq 1$, which is inconsistent with our measurements (Figure 2B). Additionally, these two previously proposed mechanisms invoked a reductive quenching of *Ir(III) by thiol to generate Ir(II) and thiyl radical cation, 25 or, alternatively, oxidative quenching of *Ir(III) by Ni(II) to generate Ni(I) and Ir(IV) (Scheme 1A).⁴⁴ Based on the relative k_q values in Table 2, we found that the initial step subsequent to photoexcitation of Ir(III) predominantly involves the reductive quenching of *Ir(III) by I to generate Ir(II) and $I \cdot .$ The rapid sequestration of $I \cdot by I^-$ to generate $I_2 \bullet^-$ with a rate constant close to the diffusional limit $(k_0)^{53}$ carries the benefit of suppressing the back-electron transfer between I. and Ir(II), which is propagated to the self-sustaining Ni(I/III) catalytic cycle (Figure 6, green cycle) via pyridinium redox mediation (Figure 6, blue cycle). Moreover, the thiyl radical in the 'radical' mechanism, whose presence was inferred from reported trapping experiments²⁵ and corroborated by our TA studies (Figure 4), was previously proposed to be generated by direct quenching of *Ir(III) and oncycle with nickel cross-coupling catalysis (Scheme 1A, top path).²⁵ In contrast, we discovered that the radical may be generated by its PCET reaction with I₂• (Figure 4) and, most importantly, is not required for the nickel cross-coupling catalytic cycle (Figure 6).

Our mechanistic insights, together with well-defined kinetics of the complete photoredox cycle, enable the optimization of the cross-coupling reaction as follows: (1) The induction period in the reaction, which is in part due to the absence of efficient quenchers of *Ir(III) to generate Ir(II) (Table 2 except pyHI), is significantly diminished by the addition of 50 mM pyHI (Figure 2A); (2) the

overall reaction efficiency and quantum yields are improved by introducing pyHI to mediate the formation of the on cycle **Ni(I)** intermediate; and, (3) notably, adding iodide to the initial reaction circumvents the requirement of substrate to provide an iodide source, thus allowing for aryl bromides to become effective substrates (Table 3). This expansion of the substrate scope increases the utility of the methodology since aryl bromides typically exhibit greater stability and commercial availability when compared to their iodo-counterparts, which may exhibit unwanted reactivity in multistep synthetic pathways.

Conclusion

Combining Stern-Volmer quenching studies, quantum yield measurements and nanosecond TA spectroscopy, we have identified the productive reaction pathways along with critical reaction intermediates and rate constants for photoredox nickelcatalyzed cross-coupling between thiols and aryl halides. We have found that a self-sustained Ni(I/III) cycle is operative for product formation, in contrast to previously proposed closed photocycles involving Ni(I), Ni(II), and Ni(III) states. In addition to identifying the productive cycle, we also determined that pyHI formed in situ serves three crucial roles in facilitating the cross-coupling reaction: (1) I⁻ serves as an effective quencher for *Ir(III) to form I• and the highly reducing Ir(II); (2) pyH+ serves as an electron shuttle between Ir(II) and Ni(II) to form Ir(III) and Ni(I) through the intermediacy of pyH•; and (3) pyH⁺ prevents formation of nickel thiolate complexes, which would interfere with the light absorption of Ir(III) via an inner filter effect. Knowledge of these reaction pathways and the roles of pyHI allowed us to optimize the reaction efficiency and expand the substrate scope from aryl iodides to include aryl bromides, thus broadening the applicability of photoredox C-S cross-coupling chemistry. The broader deployment of redox mediators such as $I^-/I_2 \bullet^-$ and $pyH^+/pyH \bullet$ may merit further investigation and can provide a general strategy for future photoredox methods development. In summary, this study demonstrates an example of how mechanistic understanding of complex photoredox systems can inform the optimization and development of photoredox reaction methodologies.

ASSOCIATED CONTENT

Supporting Information. Materials and methods, data analysis, photoredox catalysis setups, quenching studies, TA kinetics, controls and reaction optimizations.

AUTHOR INFORMATION

Corresponding Author

*Daniel G. Nocera – Department of Chemistry and Chemical Biology, Harvard University, 12 Oxford Street, Cambridge, MA 02138–2902; orcid.org/0000-0001-5055-320X; E-mail: dnocera@fas.harvard.edu.

Author

Yangzhong Qin – Department of Chemistry and Chemical Biology, Harvard University, 12 Oxford Street, Cambridge, MA 02138–2902; orcid.org/0000-0002-2450-521X.

Rui Sun – Department of Chemistry and Chemical Biology, Harvard University, 12 Oxford Street, Cambridge, MA 02138–2902; orcid.org/0000-0002-3894-8425.

Nikolas P. Gianoulis – Department of Chemistry and Chemical Biology, Harvard University, 12 Oxford Street, Cambridge, MA 02138–2902.

Author Contributions

‡ These authors contributed equally.

Funding Sources

This work was supported by the National Science Foundation under grant CHE-1855531.

Notes

The authors declare no competing financial interest.

ACKNOWLEDGMENT

We would like to thank Drs. Adam Rieth, Miguel Gonzalez, and Qilei Zhu for insightful discussions.

REFERENCES

- Twilton, J.; Le, C.; Zhang, P.; Shaw, M. H.; Evans, R. W.; MacMillan, D. W. C., The Merger of Transition Metal and Photocatalysis. *Nat. Rev. Chem.* 2017, 1, 0052.
- (2) Tellis, J. C.; Kelly, C. B.; Primer, D. N.; Jouffroy, M.; Patel, N. R.; Molander, G. A., Single-Electron Transmetalation via Photoredox/Nickel Dual Catalysis: Unlocking a New Paradigm for sp³-sp² Cross-Coupling. Acc. Chem. Res. 2016, 49, 1429-1439.
- (3) Ghosh, I.; Marzo, L.; Das, A.; Shaikh, R.; Konig, B., Visible Light Mediated Photoredox Catalytic Arylation Reactions. Acc. Chem. Res. 2016, 49, 1566-1577
- (4) Levin, M. D.; Kim, S.; Toste, F. D., Photoredox Catalysis Unlocks Single-Electron Elementary Steps in Transition Metal Catalyzed Cross-Coupling. ACS Cent. Sci. 2016, 2, 293-301.
- (5) Diccianni, J. B.; Diao, T. N., Mechanisms of Nickel-Catalyzed Cross-Coupling Reactions. Trends Chem. 2019, 1, 830-844.
- (6) Hossain, A.; Bhattacharyya, A.; Reiser, O., Copper's Rapid Ascent in Visible-Light Photoredox Catalysis. Science 2019, 364, eaav9713.
- (7) McAtee, R. C.; McClain, E. J.; Stephenson, C. R. J., Illuminating Photoredox Catalysis. Trends Chem. 2019, 1, 111-125.
- (8) Hockin, B. M.; Li, C. F.; Robertson, N.; Zysman-Colman, E., Photoredox Catalysts Based on Earth-Abundant Metal Complexes. *Catal. Sci. Technol.* 2019, 9, 889-915.
- (9) Tlahuext-Aca, A.; Hopkinson, M. N.; Daniliuc, C. G.; Glorius, F., Oxidative Addition to Gold(I) by Photoredox Catalysis: Straightforward Access to Diverse (C,N)-Cyclometalated Gold(III) Complexes. Chem. Eur. J. 2016, 22, 11587-11592.
- (10) Reed, N. L.; Herman, M. I.; Miltchev, V. P.; Yoon, T. P., Photocatalytic Oxyamination of Alkenes: Copper(II) Salts as Terminal Oxidants in Photoredox Catalysis. Org. Lett. 2018, 20, 7345-7350.
- (11) Ackerman, L. K. G.; Alvarado, J. I. M.; Doyle, A. G., Direct C-C Bond Formation from Alkanes Using Ni-Photoredox Catalysis. J. Am. Chem. Soc. 2018, 140, 14059-14063.
- (12) Shimomaki, K.; Murata, K.; Martin, R.; Iwasawa, N., Visible-Light-Driven Carboxylation of Aryl Halides by the Combined Use of Palladium and Photoredox Catalysts. J. Am. Chem. Soc. 2017, 139, 9467-9470.
- (13) Yoo, W. J.; Tsukamoto, T.; Kobayashi, S., Visible-Light-Mediated Chan-Lam Coupling Reactions of Aryl Boronic Acids and Aniline Derivatives. Angew. Chem. Int. Ed. 2015, 54, 6587-6590.
- (14) He, J.; Chen, C. Y.; Fu, G. C.; Peters, J. C., Visible-Light-Induced, Copper-Catalyzed Three-Component Coupling of Alkyl Halides, Olefins, and Trifluoromethylthiolate to Generate Trifluoromethyl Thioethers. ACS Catal. 2018, 8, 11741-11748.
- (15) Zhang, G. T.; Liu, C.; Yi, H.; Meng, Q. Y.; Bian, C. L.; Chen, H.; Jian, J. X.; Wu, L. Z.; Lei, A. W., External Oxidant-Free Oxidative Cross-Coupling: A Photoredox Cobalt-Catalyzed Aromatic C-H Thiolation for Constructing C-S Bonds. J. Am. Chem. Soc. 2015, 137, 9273-9280.
- (16) Hartwig, J. F., Carbon-Heteroatom Bond Formation Catalysed by Organometallic Complexes. *Nature* 2008, 455, 314-322.

- (17) Park, B. Y.; Pirnot, M. T.; Buchwald, S. L., Visible Light-Mediated (Hetero)Aryl Amination Using Ni(II) Salts and Photoredox Catalysis in Flow: A Synthesis of Tetracaine. J. Org. Chem. 2020, 85, 3234-3244.
- (18) Lim, C. H.; Kudisch, M.; Liu, B.; Miyake, G. M., C-N Cross-Coupling via Photoexcitation of Nickel-Amine Complexes. J. Am. Chem. Soc. 2018, 140, 7667-7673.
- (19) Key, R. J.; Vannucci, A. K., Nickel Dual Photoredox Catalysis for the Synthesis of Aryl Amines. Organometallics 2018, 37, 1468-1472.
- (20) Corcoran, E. B.; Pirnot, M. T.; Lin, S. S.; Dreher, S. D.; DiRocco, D. A.; Davies, I. W.; Buchwald, S. L.; MacMillan, D. W. C., Aryl Amination Using Ligand-Free Ni(II) Salts and Photoredox Catalysis. *Science* 2016, 353, 279-283
- (21) Terrett, J. A.; Cuthbertson, J. D.; Shurtleff, V. W.; MacMillan, D. W. C., Switching on Elusive Organometallic Mechanisms with Photoredox Catalysis. *Nature* 2015, 524, 330-334.
- (22) Welin, E. R.; Le, C.; Arias-Rotondo, D. M.; McCusker, J. K.; MacMillan, D. W. C., Photosensitized, Energy Transfer-Mediated Organometallic Catalysis through Electronically Excited Nickel (II). Science 2017, 355, 380-384.
- (23) Kim, T.; McCarver, S. J.; Lee, C.; MacMillan, D. W. C., Sulfonamidation of Aryl and Heteroaryl Halides through Photosensitized Nickel Catalysis. Angew. Chem. Int. Ed. 2018, 57, 3488-3492.
- (24) Jouffroy, M.; Kelly, C. B.; Molander, G. A., Thioetherification via Photoredox/Nickel Dual Catalysis. Org. Lett. 2016, 18, 876-879.
- (25) Oderinde, M. S.; Frenette, M.; Robbins, D. W.; Aquila, B.; Johannes, J. W., Photoredox Mediated Nickel Catalyzed Cross-Coupling of Thiols with Aryl and Heteroaryl Iodides via Thiyl Radicals. J. Am. Chem. Soc. 2016, 138, 1760-1763.
- (26) Shields, B. J.; Kudisch, B.; Scholes, G. D.; Doyle, A. G., Long-Lived Charge-Transfer States of Nickel(II) Aryl Halide Complexes Facilitate Bimolecular Photoinduced Electron Transfer. J. Am. Chem. Soc. 2018, 140, 3035-3039.
- (27) Ting, S. I.; Garakyaraghi, S.; Taliaferro, C. M.; Shields, B. J.; Scholes, G. D.; Castellano, F. N.; Doyle, A. G., 3d-d Excited States of Ni(II) Complexes Relevant to Photoredox Catalysis: Spectroscopic Identification and Mechanistic Implications. J. Am. Chem. Soc. 2020, 142, 5800-5810.
- (28) Yin, H. L.; Fu, G. C., Mechanistic Investigation of Enantioconvergent Kumada Reactions of Racemic Alpha-Bromoketones Catalyzed by a Nickel/Bis(Oxazoline) Complex. J. Am. Chem. Soc. 2019, 141, 15433-15440.
- (29) Sun, R.; Qin, Y.; Ruccolo, S.; Schnedermann, C.; Costentin, C.; Nocera, D. G., Elucidation of a Redox-Mediated Reaction Cycle for Nickel-Catalyzed Cross Coupling. J. Am. Chem. Soc. 2019, 141, 89-93.
- (30) Till, N. A.; Tian, L.; Dong, Z.; Scholes, G. D.; MacMillan, D. W. C., Mechanistic Analysis of Metallaphotoredox C-N Coupling: Photocatalysis Initiates and Perpetuates Ni(I)/Ni(III) Coupling Activity. J. Am. Chem. Soc. 2020, 142, 15830-15841.
- (31) Jarrett, J. T., The Biosynthesis of Thiol- and Thioether-Containing Cofactors and Secondary Metabolites Catalyzed by Radical S-Adenosylmethionine Enzymes. J. Biol. Chem. 2015, 290, 3972-3979.
- (32) Ilardi, E. A.; Vitaku, E.; Njardarson, J. T., Data-Mining for Sulfur and Fluorine: An Evaluation of Pharmaceuticals to Reveal Opportunities for Drug Design and Discovery. J. Med. Chem. 2014, 57, 2832-2842.
- (33) Scott, K. A.; Njardarson, J. T., Analysis of Us Fda-Approved Drugs Containing Sulfur Atoms. Top. Curr. Chem. 2018, 376.
- (34) Feng, M. H.; Tang, B. Q.; Liang, S. H.; Jiang, X. F., Sulfur Containing Scaffolds in Drugs: Synthesis and Application in Medicinal Chemistry. Curr. Top. Med. Chem. 2016, 16, 1200-1216.
- (35) Eichman, C. C.; Stambuli, J. P., Transition Metal Catalyzed Synthesis of Aryl Sulfides. Molecules 2011, 16, 590-608.
- (36) Fernandez-Rodriguez, M. A.; Shen, Q. L.; Hartwig, J. F., A General and Long-Lived Catalyst for the Palladium-Catalyzed Coupling of Aryl Halides with Thiols. J. Am. Chem. Soc. 2006, 128, 2180-2181.
- (37) Murata, M.; Buchwald, S. L., A General and Efficient Method for the Palladium-Catalyzed Cross-Coupling of Thiols and Secondary Phosphines. *Tetrahedron* 2004, 60, 7397-7403.
- (38) Ke, F.; Qu, Y. Y.; Jiang, Z. Q.; Li, Z. K.; Wu, D.; Zhou, X. G., An Efficient Copper-Catalyzed Carbon-Sulfur Bond Formation Protocol in Water. Org. Lett. 2011, 13, 454-457.

- (39) Qiao, Z. J.; Wei, J. P.; Jiang, X. F., Direct Cross-Coupling Access to Diverse Aromatic Sulfide: Palladium-Catalyzed Double C-S Bond Construction Using Na₂S₂O₃ as a Sulfurating Reagent. Org. Lett. 2014, 16, 1212-1215.
- (40) Wang, X.; Cuny, G. D.; Noel, T., A Mild, One-Pot Stadler-Ziegler Synthesis of Arylsulfides Facilitated by Photoredox Catalysis in Batch and Continuous-Flow. Angew. Chem. Int. Ed. 2013, 52, 7860-7864.
- (41) Liu, B.; Lim, C. H.; Miyake, G. M., Visible-Light-Promoted C-S Cross-Coupling via Intermolecular Charge Transfer. J. Am. Chem. Soc. 2017, 139, 13616-13619.
- (42) Jiang, M.; Li, H. F.; Yang, H. J.; Fu, H., Room-Temperature Arylation of Thiols: Breakthrough with Aryl Chlorides. Angew. Chem. Int. Ed. 2017, 56, 874-879
- (43) Sikari, R.; Sinha, S.; Das, S.; Saha, A.; Chakraborty, G.; Mondal, R.; Paul, N. D., Achieving Nickel Catalyzed C-S Cross-Coupling under Mild Conditions Using Metal Ligand Cooperativity. J. Org. Chem. 2019, 84, 4072-4085.
- (44) Ren, H.; Li, G. F.; Zhu, B.; Lv, X. D.; Yao, L. S.; Wang, X. L.; Su, Z. M.; Guan, W., How Does Iridium(III) Photocatalyst Regulate Nickel(II) Catalyst in Metallaphotoredox-Catalyzed C-S Cross-Coupling? Theoretical and Experimental Insights. ACS Catal. 2019, 9, 3858-3865.
- (45) Sun, R.; Qin, Y.; Nocera, D. G., General Paradigm in Photoredox Ni-Catalyzed Cross-Coupling Allows for Light-Free Access to Reactivity. Angew. Chem. Int. Ed. 2020, 59, 2-9.
- (46) Qin, Y. Z.; Martindale, B. C. M.; Sun, R.; Rieth, A. J.; Nocera, D. G., Solar-Driven Tandem Photoredox Nickel-Catalysed Cross-Coupling Using Modified Carbon Nitride. Chem. Sci. 2020, 11, 7456-7461.
- (47) Hatchard, C. G.; Parker, C. A., A New Sensitive Chemical Actinometer II. Potassium Ferrioxalate as a Standard Chemical Actinometer. Proc. R. Soc. London, Ser. A 1956, 235, 518-536.
- (48) Holder, P. G.; Pizano, A. A.; Anderson, B. L.; Stubbe, J.; Nocera, D. G., Deciphering Radical Transport in the Large Subunit of Class I Ribonucleotide Reductase. J. Am. Chem. Soc. 2012, 134, 1172-1180.
- (49) Miller, D. C.; Choi, G. J.; Orbe, H. S.; Knowles, R. R., Catalytic Olefin Hydroamidation Enabled by Proton-Coupled Electron Transfer. J. Am. Chem. Soc. 2015, 137, 13492-13495.
- (50) Qiu, G. Q.; Knowles, R. R., Understanding Chemoselectivity in Proton-Coupled Electron Transfer: A Kinetic Study of Amide and Thiol Activation. J. Am. Chem. Soc. 2019, 141, 16574-16578.
- (51) Ruccolo, S.; Qin, Y. Z.; Schnedermann, C.; Nocera, D. G., General Strategy for Improving the Quantum Efficiency of Photoredox Hydroamidation Catalysis. J. Am. Chem. Soc. 2018, 140, 14926-14937.
- (52) Kolthoff, I. M.; Chantooni, M. K.; Bhowmik, S., Dissociation Constants of Uncharged and Monovalent Cation Acids in Dimethyl Sulfoxide. J. Am. Chem. Soc. 1968, 90, 23-28.
- (53) Gardner, J. M.; Abrahamsson, M.; Farnum, B. H.; Meyer, G. J., Visible Light Generation of Iodine Atoms and I-I Bonds: Sensitized I⁻ Oxidation and I₃⁻ Photodissociation. J. Am. Chem. Soc. 2009, 131, 16206-16214.
- (54) Wang, X. G.; Stanbury, D. M., Oxidation of Iodide by a Series of Fe(III) Complexes in Acetonitrile. *Inorg. Chem.* 2006, 45, 3415-3423.
- (55) Keith, J. A.; Carter, E. A., Theoretical Insights into Pyridinium-Based Photoelectrocatalytic Reduction of CO₂. J. Am. Chem. Soc. 2012, 134, 7580-7583.
- (56) Lim, C. H.; Holder, A. M.; Hynes, J. T.; Musgrave, C. B., Reduction of CO₂ to Methanol Catalyzed by a Biomimetic Organo-Hydride Produced from Pyridine. J. Am. Chem. Soc. 2014, 136, 16081-16095.
- (57) Elliot, A. J., A Pulse-Radiolysis Study of the Reaction of OH with I₂ and the Decay of I₂⁻. Can. J. Chem. 1992, 70, 1658-1661.
- (58) Cukier, R. I.; Nocera, D. G., Proton-Coupled Electron Transfer. Annu. Rev. Phys. Chem. 1998, 49, 337-369.
- (59) Reece, S. Y.; Nocera, D. G., Proton-Coupled Electron Transfer in Biology: Results from Synergistic Studies in Natural and Model Systems. Annu. Rev. Biochem 2009, 78, 673-699.
- (60) Tsou, T. T.; Kochi, J. K., Mechanism of Oxidative Addition Reaction of Nickel(0) Complexes with Aromatic Halides. J. Am. Chem. Soc. 1979, 101, 6319-6332.
- (61) Amatore, C.; Jutand, A., Rates and Mechanisms of Electron-Transfer Nickel-Catalyzed Homocoupling and Carboxylation Reactions. An Electrochemical Approach. Acta Chem. Scand. 1990, 44, 755-764.
- (62) Cole, E. B.; Lakkaraju, P. S.; Rampulla, D. M.; Morris, A. J.; Abelev, E.; Bocarsly, A. B., Using a One-Electron Shuttle for the Multielectron

- Reduction of CO₂ to Methanol: Kinetic, Mechanistic, and Structural Insights. J. Am. Chem. Soc. 2010, 132, 11539-11551.
- (63) Lebegue, E.; Agullo, J.; Belanger, D., Electrochemical Behavior of Pyridinium and N-Methyl Pyridinium Cations in Aqueous Electrolytes for CO₂ Reduction. ChemSusChem 2018, 11, 219-228.
- (64) Han, D. Y.; Li, S. S.; Xia, S. Q.; Su, M. C.; Jin, J., Nickel-Catalyzed Amination of (Hetero)Aryl Halides Facilitated by a Catalytic Pyridinium Additive. Chem. Eur. J. 2020, 26, 12349-12354.

